Nanographene-based decoration as a panchromatic antenna for metalloporphyrin conjugates

Saül Garcia-Orrit, Victor Vega-Mayoral, Qiang Chen, Gianluca Serra, Giuseppe M. Paternò, Enrique Cánovas, Akimitsu Narita, Klaus Müllen, Matteo Tommasini, Juan Cabanillas-González

Nanographene-based decoration as a panchromatic antenna for metalloporphyrin conjugates

Saül Garcia-Orrit,[a†] Victor Vega-Mayoral,[a†] Qiang Chen,[b] Gianluca Serra,[c] Giuseppe M. Paternò,[d] Enrique Cánovas,[a] Akimitsu Narita,[b,e] Klaus Müllen,[b,f] Matteo Tommasini,[c] Juan Cabanillas-González,[a*]*

[a] Madrid Institute for Advanced Studies, IMDEA Nanociencia, c/Faraday 9, Campus de Cantoblanco, Madrid 28049, Spain

[b] Max Planck Institute for Polymer Research, Ackermannweg 10, 55128 Mainz, Germany

[c] Dipartimento di Chimica, Materiali ed Ingegneria Chimica "G.Natta", Politecnico di Milano, Piazza Leonardo da Vinci 32, Milano 20133, Italy

[d] Physics Department, Politecnico di Milano, Piazza Leonardo Da Vinci, 32, 20133 Milano, Italy

[e] Organic and Carbon Nanomaterials Unit, Okinawa Institute of Science and Technology Graduate University, Okinawa 904-0495, Japan

[f] Institute for Physical Chemistry, Johannes Gutenberg University Mainz, Duesbergweg 10-14, 55128 Mainz, Germany

[†] Equally contributing authors

E-mail: juan.cabanillas@imdea.org, matteo.tommasini@polimi.it

Keywords: nanographenes, panchromatic, organic solar cells, photocatalysis, metalloporphyrins, redox, solar fuels.

Porphyrins, a type of heterocyclic aromatic compounds consisting of tetrapyrroles connected by four substituted methine groups, are appealing building blocks for solar energy applications. However, their photosensitization capability is limited by their large optical energy gap, which results in a mismatch in absorption towards efficient harvesting of the solar spectrum. Porphyrin π-extension by edge-fusing with nanographenes can be employed for narrowing their optical energy gap from 2.35 eV to 1.08 eV, enabling the development of porphyrin-based panchromatic dyes with an optimized energy onset for solar energy conversion in dye-sensitized solar fuel and solar cell configurations. By combining time-dependent density functional theory with femtosecond transient absorption spectroscopy we find that the primary singlets, which are delocalized across the entire aromatic part, are transferred into metal centred triplets in only 1.2 ps, and subsequently relax towards ligand-delocalized triplets. This observation implies that the decoration of the porphyrin moiety with nanographenes, while having a large impact on the absorption onset of the novel dye, promotes the formation of a ligand-centred lowest triplet state of large spatial extension, potentially interesting for boosting interactions with electron scavengers. These results reveal a design strategy for broadening the applicability of porphyrin-based dyes in optoelectronics.

1. Introduction

Control of excited state dynamics in chromophores is a crucial aspect for optimizing photoconversion efficiency in organic-based solar cell and solar fuel architectures. For example, understanding and eventually fine-tuning charge carrier dynamics in molecular dyes is key to facilitate electron-transfer reactions in donor-acceptor systems, where transferred electrons can subsequently trigger catalytic activity. [1–3] Typical examples of light induced catalysis based on these architectures are water splitting to produce hydrogen for fuel cells [4–7] and/or CO_2 reduction to achieve high added-value chemicals. [8,9] Within this context, harnessing parallel electronic decay pathways that detrimentally compete with the targeted photochemical reaction is crucial to improve photoconversion efficiency. Among currently available solutions, transition metal complexes have been widely exploited toward that end, owing to long-lived photoexcited electron dynamics, enabled by rapid inter-system crossing in the picosecond to sub-picosecond timescale to the triplet state. [10,11] Within this family of compounds, open-shell metalloporphyrins, such as nickel(II) porphyrins, depict these described advantages, as primary porphyrin-centred excited states relax rapidly towards a

metal centred triplet, enabling the photogenerated electron to be employed for a catalytic reaction prior to decaying to the ground state.[1,10–12] Apart from this desirable feature, Ni porphyrins have demonstrated to be very stable under catalytic conditions, being able to survive the harsh (strongly acidic) reaction conditions employed for their synthesis,[12] or in operando in solar fuel configurations.[13] Further research on these compounds include the usage of porphyrin-based metal-organic frameworks (MOFs), which exhibit excellent photocatalytic reduction of CO_2. [14,15] Despite the appealing features of porphyrins acting as chemical reaction centers, their capability for harvesting sunlight is largely limited to the ultraviolet region (UV) of the solar spectrum, i.e., their capability to absorb photons in the green-to-near infrared, where most sunlight photons are available, is very limited. In this respect, an appealing target is to realize novel dyes where the porphyrin absorption spectrum is extended [16,17] while preserving the rest of the appealing features; as e.g., avoiding an impact over the intermediate relaxation pathways and the final yield of the reactive excited states. Following this aim, previous reports showed approaches where small polycyclic aromatic hydrocarbons were fused to the porphyrin periphery, developing π-extended porphyrins with red-shifted absorption onsets toward the near-infrared (NIR).[16,17] More recently, some of us reported on the synthesis of a 5,15-(dimesityl)porphyrin nickel(II) (**NiDMP**) fused in a symmetric fashion with two nanographenes (named hereafter **NPN**) as shown in Figure 1, in which the nanographenes are hexa-*peri*-hexabenzocoronenes having two K-regions on the neighboring bay positions [18]. The choice of Ni(II) as open shell metal at the porphyrin center instead of Zn(II) or Co(II) is for the stabilization of the porphyrin core during the synthesis of the **NPN** conjugate, which involves an oxidative and acidic reaction condition.[18] The obtained planar structure of **NPN** enhances π-conjugation between the porphyrin and the fused nanographene moieties, which further results in a broad absorption spectrum spanning across the entire visible region. The **NPN** absorption spans up to 1200 nm, well beyond the 800-900 nm absorption limit of porphyrin-based dyads previously reported. [16,17,19–22] The extended planarity and the large size of the nanographenes are key to achieve this outstanding panchromatic behavior. Moreover, the three C-C bonds that completely fuse the nanographenes to the Ni porphyrin core not only enable electron delocalization, but also extend the heavy atom-effect of Ni to the entire nanographene-porphyrin structure. Thus, combination of aromatic fusing and heavy metal atom inclusion can provide possibilities towards introducing spin properties in polycyclic aromatic hydrocarbons. In this work, we explore the exciton dynamics in **NPN** by combining time-dependent density functional theory (TDDFT) and femtosecond transient absorption

spectroscopy (TAS). Our results confirm the presence of an ultrafast energy transfer from the nanographene-porphyrin moiety towards the porphyrin metal center, which subsequently relaxes into a π-extended state. These findings show an avenue for extending the absorption spectra of porphyrins towards the near infrared via nanographene decoration while providing spatial extension to promote interactions with electron scavengers. Extending the bandgap towards the infrared is a key target towards higher photoconversion efficiencies in sensitized architectures, this critical aspect should, in any case, be accompanied by an engineered donor-acceptor interface where energetics and excited electron kinetics favor photoinduced charge transfer. [23] These findings set the basis for improving the applicability of porphyrin-based compounds to solar energy conversion schemes.

2. Results and discussion

2.1 Experimental and simulated UV-Vis absorption spectra

TDDFT calculations allow to reliably simulate the absorption spectra of both **NiDMP** and **NPN**, as shown in Figure 1. To keep the computational burden under control we described C, N, and H atoms with the 6-31G(d,p) basis set and the Ni atom with Ahlrichs VTZ basis set. This choice closely follows a previous computational work on Ni porphyrin [24]. As for the choice of the DFT functionals, we found that the combination of B3LYP to determine the ground state equilibrium structure and PBE to compute the vertical transitions by TDDFT was accurate enough for our purposes. This outcome is also consistent with previous works on Ni porphyrins [24–26] (further details are reported in SI). The Soret band of **NiDMP** is observed at 401 nm and it is computed at 404 nm. It is assigned to electronic transitions involving delocalized π orbitals (see SI for details). We also obtain by TDDFT calculations the Q band at 527 nm (2.35 eV), which is reasonably close to the peak found in the experimental UV-Vis spectrum at 517 nm (2.40 eV). TDDFT calculations in **NPN** also provide a good description of the UV-Vis absorption profile (Figure 1). The position of S_1 (1182 nm, 1.05 eV) is well accounted by the theory (1143 nm, 1.08 eV). The experimental peak observed at 994 nm (1.25 eV) is assigned to the 0→1 vibronic component of S_1. This is based on the fact that the vibronic spacing between 1.25 eV and 1.05 eV (1613 cm^{-1}) approaches the position of the G band in the Raman spectrum of **NPN** [25], for which we expect a sizeable vibronic coupling based on the geometry relaxation pattern computed between the minima of the GS and S_1. As reported in the SI, the relaxation pattern shows large displacements along CC stretching

coordinates whose involvement is expected in G modes. The other **NPN** broad absorption band at 605 nm (2.05 eV) corresponds to two rather close transitions computed by TDDFT at 575 nm (2.15 eV) and 610 nm (2.03 eV).

We did not observe spontaneous or stimulated emission for either **NiDMP** or **NPN** molecules, in contrast to some reports claiming the presence of a SE band which decays in few picoseconds in Ni(II) porphyrin related systems. [27–29] This effect is explained as the result of ultrafast inter-system crossing due to the Ni atom inclusion. [30,31]

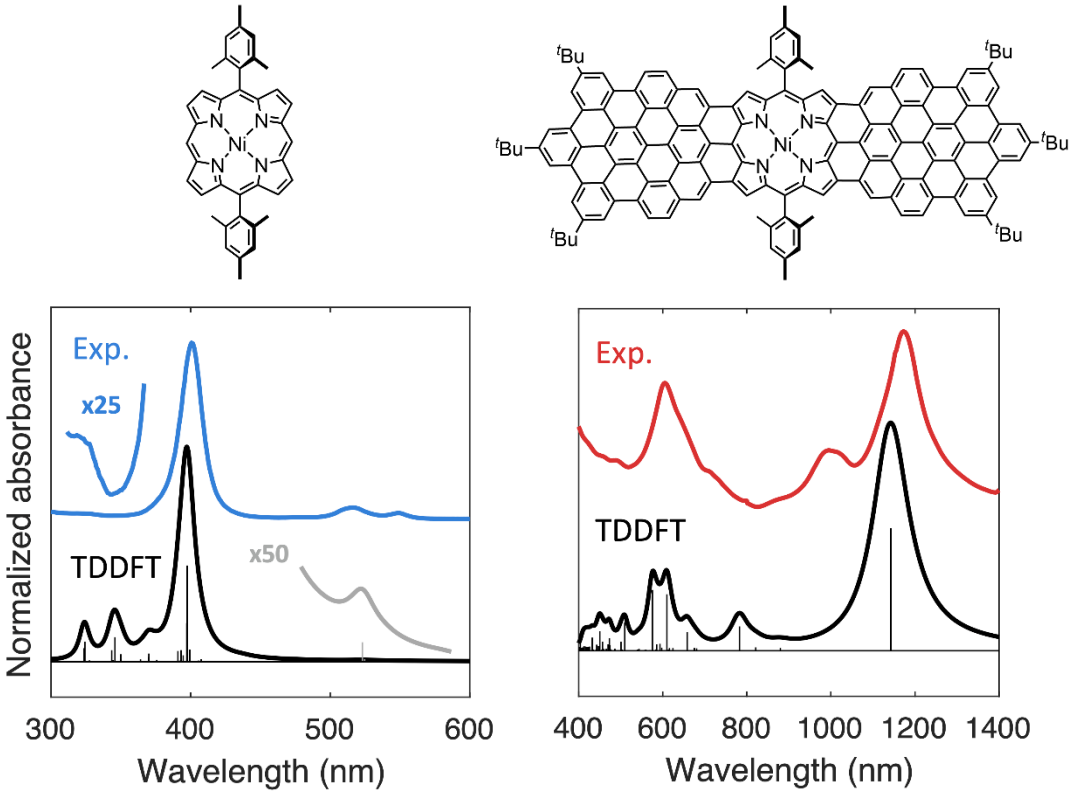

Figure 1. Computed and experimental UV-Vis absorption spectra of **NiDMP** (left) and **NPN** (right); the chemical structures of the molecules are reported as insets. The spectra have been normalized and vertically shifted for the sake of clarity. Black lines indicate the position of the computed vertical transitions whose oscillator strengths are proportional to the line height; grey lines have the same meaning but refer to the zoomed parts of the spectra.

2.2. Femtosecond transient absorption spectroscopy

To scrutinize the photophysics of **NPN**, we carried out transient absorption spectroscopy (TAS) and employed **NiDMP** as a reference sample. The pump excitation energy employed in

the TAS experiment on **NiDMP** (3.2 eV, 387 nm) excites the Soret band, whereas the excitation pump used for **NPN** (2.05 eV, 605 nm) excites a delocalized π→π* transition of the nanographene moiety, which is computed at 610 nm (see Table S2 in SI). In other words, to properly compare the excited-state dynamics of **NiDMP** and **NPN**, we excite S_2 in both cases. The decay pathways are instead probed with a supercontinuum in the 3 - 0.9 eV (430-1400 nm) energy (wavelength) range. The TAS experimental findings in **NiDMP** and **NPN** are depicted by the contour plots in Figure 2(a) and Figure 3(a) respectively, where the red and blue areas stand respectively for pump-induced reduction in ground state absorption also referred as ground state bleach (GSB, $\Delta T/T > 0$) and photoinduced absorption (PA, $\Delta T/T < 0$). Starting with **NiDMP** (Figure 2(a)), the TAS is composed (from high to low energies) of a PA region between 3.10 eV and 2.80 eV, and alternated GSB and PA in the 2.5 – 2.2 eV energy range, resembling the first derivative of the **NiDMP** Q absorption band (2.40 eV, 517 nm). This derivative-like feature was previously reported in similar metalloporphyrins and assigned to a metal centred (d,d) triplet excited state. [32] In turn, the **NPN** TAS signal is composed of two positive (red shaded) areas centred at 1.05 eV and 1.25 eV (Figure 3(a)), which coincide with the **NPN** absorption bands at 1182 and 994 nm respectively, being therefore assigned to GSB. In the low energy region, a PA band down to 0.93 eV due to excited state absorption is observed. Given that we did not observe any fluorescence from **NiDMP** or **NPN** and bearing in mind the interplay of triplets in the electron relaxation pathways of related metalloporphyrins, [25,26] we attempted to reconstruct the TAS spectra and dynamics with different photophysical models, observing a good agreement only when a linear chain reaction is invoked, which involves inter-system crossing from S_1 without competition with a parallel S_1-S_0 decay channel. Noteworthy, the linear reaction proposed to fit the data is consistent with the absence of fluorescence in **NiDMP** or **NPN**. The proposed photophysical scenario, common for **NiDMP** and **NPN**, involves photoexcitation of a primary ligand-centred singlet level which undergoes intersystem crossing towards a non-thermalized triplet level, relaxation to the lowest triplet state and ground state decay. This four-level sequential model is implicit in the following set of coupled equations:

$$\boldsymbol{dN_S/dt = g - k_S N_S} \quad (1)$$

$$\boldsymbol{dN_{T'}/dt = k_s N_s - k_{T'} N_{T'}} \quad (2)$$

$$\boldsymbol{dN_{T1}/dt = k_{T'} N_{T'} - k_{T1} N_{T1}} \quad (3)$$

$$\boldsymbol{dN_g/dt = k_{T1} N_{T1} - g} \quad (4)$$

where, N_S, $N_{T'}$, N_{T1} stand for the time-dependent population of singlets, non-thermalized (T´) and thermalized (T_1) triplets respectively, whereas k_S, $k_{T'}$ and k_{T1} are their corresponding decay rates. The ground state population (N_g) is depleted by the photoexcitation with an impulsive-like rate g. A comparison between the experimental and global fitted TAS contour plots in Figure 2(a) and Figure 3(a) and between the TAS experimental and fitted dynamics at selected energies (Figure 2(b) and Figure 3(b)), illustrates how the model can describe the data rather well. Focusing first on **NiDMP**, photoexcitation leads to a primary singlet which undergoes intersystem crossing in 0.8 ps towards an upper T´ triplet level, followed by thermalization in 16 ps to the lowest T_1 triplet level and decay to the ground state in 287 ps, (Figure 2(c)). Noteworthy, these three decay components are in good agreement with ~1 ps, ~20 ps and ~200 ps respectively reported by Chen et al. and Shelby et al. on **NiTMP** with the same photophysical model, the first one under identical photoexcitation conditions.[25,26] In turn, the excited-state deactivation pathways in **NPN** (Figure 3(c)) involve intersystem crossing in 1.2 ps towards an upper lying T´**,** thermalization and ground state decay in 18 ps and 100 ps respectively, namely an almost three-fold reduction respect to ground state decay in **NiDMP**, pointing to additional non-radiative triplet decay channels. TAS spectra and kinetics are closely modelled with the same linear reaction kinetic models and similar decay rates, confirming a sequential decay reaction in both compounds. In the next section we address with TDDFT calculations the nature of the electronic states involved in the de-activation pathways and their energetic location.

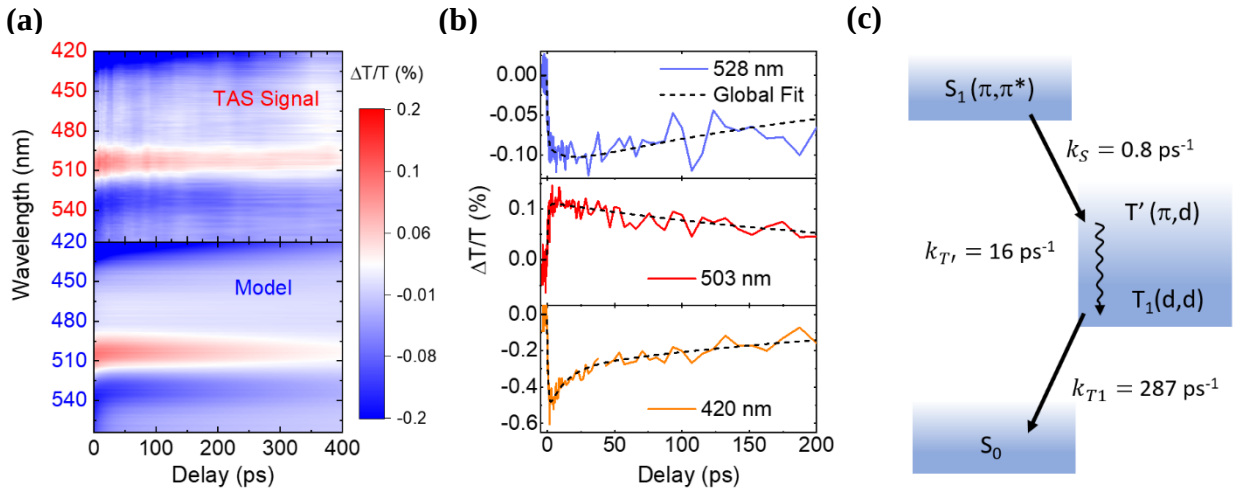

Figure 2. (a) Experimental (up) and fitted (down) TAS contour plots of **NiDMP. (b)** ΔT/T decay traces at different energies with their associated global fits obtained from the sequential model for **NiDMP. (c)** Four sequential level model scheme employed for the global fit analysis with the corresponding rate values. The electronic character of each level is based on TDDFT calculations, as well as the energy of each one (S1 [1.88 eV], T' [1.76 eV], T1 [1.01 eV], S0 [0 eV]).

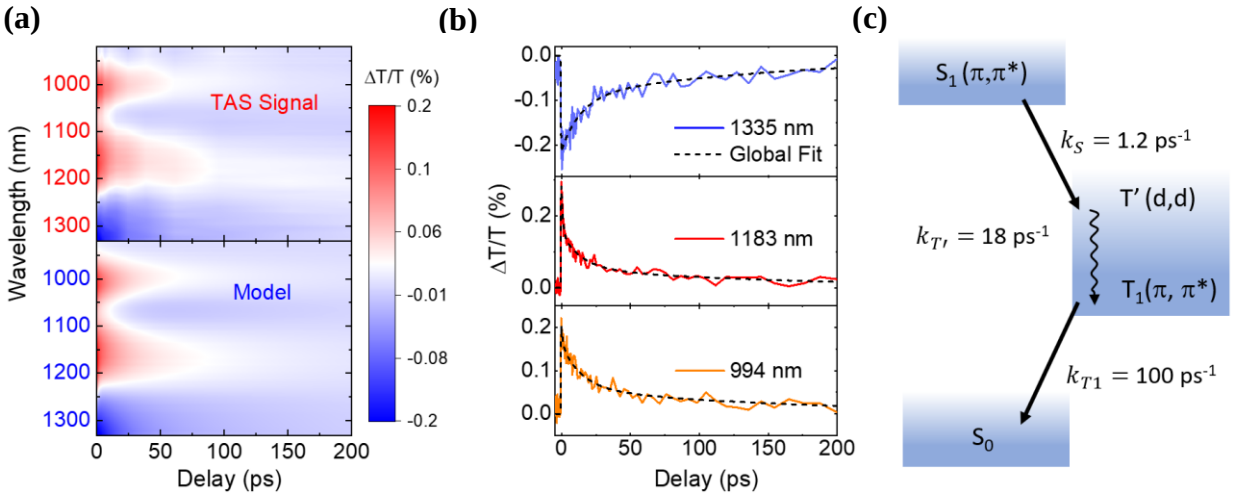

Figure 3. (a) Experimental (up) and fitted (down) TAS contour plots of **NPN. (b)** ΔT/T decay traces at different energies with their associated global fits obtained from the sequential model for **NPN. (c)** Four sequential level model scheme employed for the global fit analysis with the corresponding rate values. The electronic character of each level is based on TDDFT

calculations, as well as the energy of each one (S1 [1.08 eV], T' [0.96 eV], T1 [0.71 eV], S0 [0 eV]).

2.3. Excited state assignment and discussion

TDDFT calculations determine the energy difference between the ground state (GS) and the singlet (S_n) or triplet (T_n) excited states. Hence, the TDDFT results reported in Figure 4 have been used to support the interpretation of the deactivation pathways proposed in the analysis of the TAS measurements. In the case of **NiDMP**, by taking the GS energy as reference (0 eV) we obtain the energy of the S_1 state at 1.88 eV and the energy of the T_1 state at 1.01 eV. TDDFT calculations on **NiDMP** also reveal a pair of nearly degenerate triplets (T_2, T_3) that are computed at 1.12 eV and an upper T_4 level at 1.76 eV. T_1 is described mainly as a HOMO ($3d_{z^2}$) → LUMO ($3d_{x^2-y^2}$) transition, which is localized on the metal center as the maps of the HOMO and LUMO orbitals clearly show. Based on the labelling scheme adopted by Chen et al., [25] we label T_1 as T_1(d,d). The triplets computed at higher energies agree with the interplay of a T'(π,d) state populated by inter-system crossing from singlets, as depicted in Figure 2(c) and in line with previous reports. [26,28,31] In particular T_4 involves a transition from the HOMO-3 level which shows a minor contribution from one d orbital and a major contribution from a delocalized π orbital, leading to the T'(π,d) assignment in the deactivation pathway of **NiDMP** discussed above.

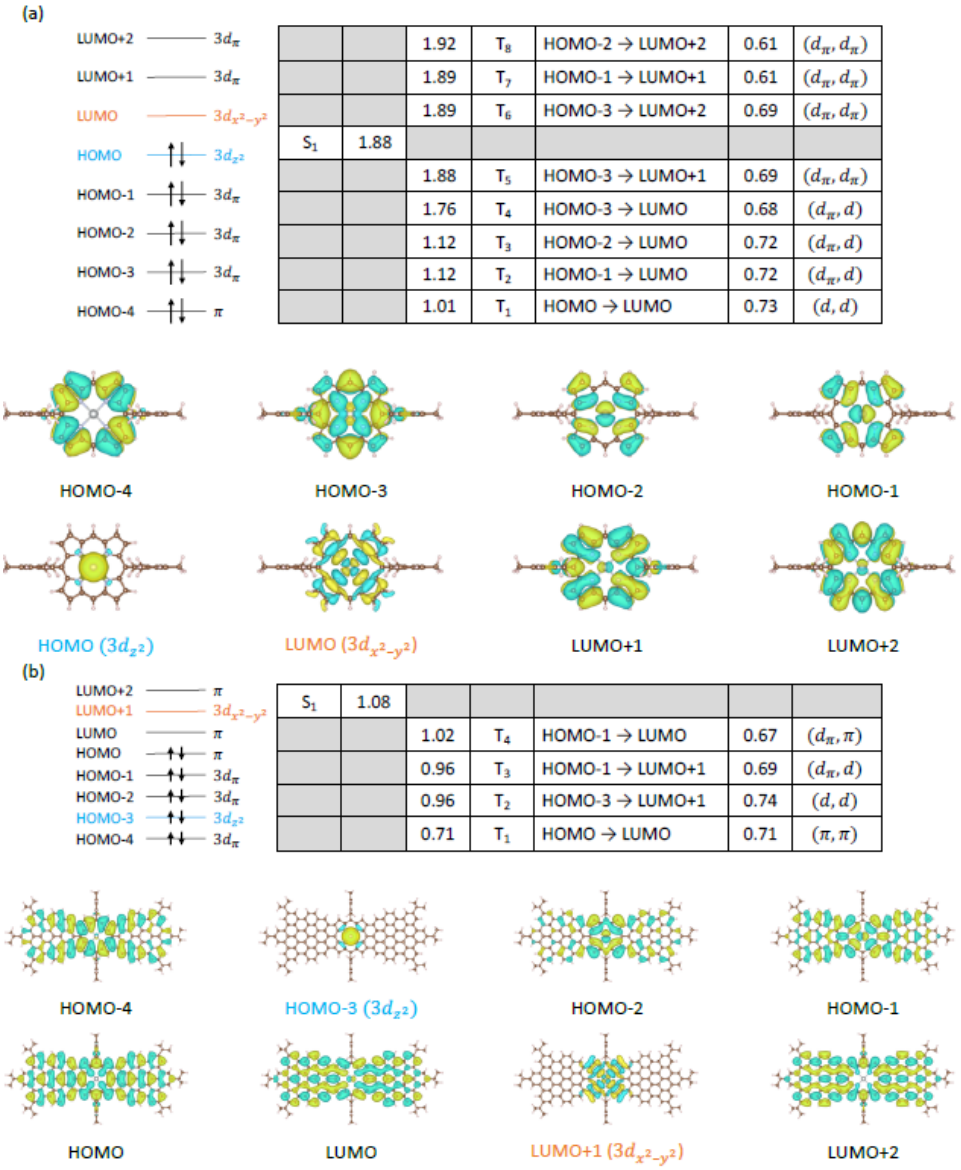

		1.92	T_8	HOMO-2 → LUMO+2	0.61	(d_π, d_π)
		1.89	T_7	HOMO-1 → LUMO+1	0.61	(d_π, d_π)
		1.89	T_6	HOMO-3 → LUMO+2	0.69	(d_π, d_π)
S_1	1.88					
		1.88	T_5	HOMO-3 → LUMO+1	0.69	(d_π, d_π)
		1.76	T_4	HOMO-3 → LUMO	0.68	(d_π, d)
		1.12	T_3	HOMO-2 → LUMO	0.72	(d_π, d)
		1.12	T_2	HOMO-1 → LUMO	0.72	(d_π, d)
		1.01	T_1	HOMO → LUMO	0.73	(d, d)

S_1	1.08					
		1.02	T_4	HOMO-1 → LUMO	0.67	(d_π, π)
		0.96	T_3	HOMO-1 → LUMO+1	0.69	(d_π, d)
		0.96	T_2	HOMO-3 → LUMO+1	0.74	(d, d)
		0.71	T_1	HOMO → LUMO	0.71	(π, π)

Figure 4. Electron configuration of **NiDMP** (a) and **NPN** (b) and their low-lying singlet and triplet states. The top left part of each panel reports the electron configuration nearby the frontier orbitals; the nature of each orbital is also specified according to ref. [26]. Light blue and orange orbitals are put in evidence since they determine localized T(d,d) states (T_1 in **NiDMP**, T_2 in **NPN**). The table in the top right compares the position of the less energetic singlet state with the lowest lying triplets: the first and second columns report the singlet state and its energy in eV; the third and fourth columns report the triplet states and their energies in eV; the fifth and sixth columns report the main transition involved in the triplet state, and its relative contribution; finally, the seventh column reports the nature of the initial and final state involved in the transition. The bottom part shows the isosurfaces of the orbitals at 0.012 $a_0^{-3/2}$ (a) or at 0.006 $a_0^{-3/2}$ (b).

The extended π-conjugation of **NPN** causes a different orbital ordering with respect to **NiDMP** (Figure 4). Upon increasing conjugation, the occupied (unoccupied) π orbitals increase (decrease) their energy in contrast to the d orbitals located on the metal centre which are expected to be weakly affected by changes in π conjugation. Indeed, the $3d_{z^2}$ orbital energy is -4.49 eV in **NPN** (HOMO-3) and -4.52 eV in **NiDMP** (HOMO), whereas the energy of the $3d_{x^2-y^2}$ orbital is -2.78 eV in both molecules (LUMO+1 in **NPN** and LUMO in **NiDMP**). Hence, the change in position of the frontier π orbitals upon increasing conjugation causes the change of the HOMO and LUMO orbitals in **NPN** from d to π. By consequence, the **NPN** triplet state localized on the nickel center (T_2) is not associated to the HOMO→LUMO transition but to the HOMO-3 ($3d_{z^2}$) → LUMO+1 ($3d_{x^2-y^2}$) transition that involves the localized d orbitals. T_2 and T_3 levels are degenerate, the latter also having a predominant metal centred character. Their energetic position (0.96 eV) approaches the T_1(d,d) energy in **NiDMP**, confirming to be insensitive to π-conjugation (Figure 4). Noteworthy, the nature and energetic position of T_2 and T_3 justifies the interplay of an upper metal centred T´(d,d) in the deactivation pathways diagram of **NPN** (Figure 3(c)). The lowest triplet state $T_1(\pi,\pi^*)$ is computed at 0.71 eV and has instead a major contribution on the ligand. Notably, electronic relaxation towards a π-π* triplet state delocalized on the ligand is a distinctive signature of **NPN** with respect to **NiDMP**.

In view of the results presented above some conclusions can be drawn. In general, the use of moieties to extend the porphyrin conjugation can potentially cause interference with the formation of the transient reactive species required to trigger a specific photochemical reaction. In this respect, it is noteworthy that triply fused functionalization of **NiDMP** with hexa-peri-hexabenzocoronenes preserves a similar ultrafast inter-system crossing rate as in **NiDMP**, eluding ground-state relaxation in the singlet manifold. The reconstruction of the **NiDMP** and **NPN** TAS data with a four-level sequential model without intermediate losses to the ground state suggests the absence of parallel decay processes in the singlet or triplet manifold. Thus, photoexcited electrons can be eventually harnessed to trigger light-to-energy conversion without facing competition with intermediate parasitic losses. It is remarkable that the lateral hexa-peri-hexabenzocoronenes and the central **NiDMP** core in **NPN** play two differentiated roles, the former aiming at extending the absorption spectral range towards the near-IR coverage whilst the latter hosting the intermediate T´(d,d) state which funnels electrons from primarily delocalized S(π,π*) states. In this way, the porphyrin core acts as an

intermediate node, from which energy re-distribution takes place. As shown by TDDFT calculations, its energetic position is decoupled from the peripheral ligands which surrounds it. Such feature could potentially allow to tune independently the absorption while maintaining intermediate reactive metal centers of interest for specific photochemical reactions. The subsequent relaxation towards a ligand delocalized state could potentially aim at enhancing chemical interactions with the surroundings. It must be noted that the triplet lifetimes in **NiDMP** and **NPN** are well below those reported in some of the most widely addressed transition metal complexes employed to trigger redox reactions, particularly those containing d^6 transition metals such as Ru(II) or Os (II) with lifetimes extending to the nano-microsecond. [33] Large redox potentials and long triplet excited state lifetimes have been identified as key factors for efficient photochemical reactions, [34,35] and for this reason, open-shell transition metals have been traditionally dismissed owing to the relatively fast decay of the triplet to the ground state. [36,37] However, the use of transition metal complexes such as Ni(II) is relevant since it has been demonstrated that photocalytic activity can be initiated on picosecond or even sub-picosecond timescales in some metal-transition complexes. [1,10–12] Besides, from the point of view of applications, the substitution of rare and expensive metals with relatively abundant and cost-effective transition metals such as Ni will become of paramount importance for the development of sustainable technologies.

3. Conclusions

Transient absorption spectroscopy and time-dependent density functional calculations were employed in the characterization of a novel (dimesityl)porphyrin nickel(II) triply fused with nanographene-based chromophores with panchromatic absorption. In this nanographene – porphyrin conjugate we unravel an ultrafast inter-system crossing towards a metal centred triplet localized at the porphyrin core, which is barely affected from the energetic point of view by functionalization. Subsequent relaxation towards a delocalized ligand centred triplet state is unravellled. These results might pave the way to a new strategy to synthesize panchromatic molecules for solar energy conversion, as the intermediate yield of the reactive excited-states is almost unnaffected by the symmetric nanographene expansion of the porphyrin center, which acts as an antenna during the electronic relaxation process, while the optical properties, and consequently the panchromaticity, likely could be tuned by varying the nanographene shape and size.

Acknowledgements

Saül Garcia-Orrit and Victor Vega-Mayoral contributed equally to this work.

J.C.G acknowledges the Spanish Ministry of Science and Innovation (PID2021-128313OB-I00), the Regional Government of Madrid through projects NMAT2D-CM (S2018/NMT-4511), Proyectos Sinérgicos de I + D (Grant Y2018/NMT-5028 FULMATEN-CM) and NANOCOV-CM (REACT-UE). V. V.-M. acknowledges financial support from the regional government of Madrid "Atracción del talento" program (2019-T2/IND-12737) and Spanish Ministry of Science and Innovation through proyectos Estratégicos Orientados a la Transición Ecológica y a la Transición Digital (TED2021-131906A-100). Q.C., A.N., and K.M. are grateful to the financial support from the Max Planck Society. Q.C. and A.N. appreciate the financial support from the ANR-DFG NLE Grant GRANAO by DFG 431450789. K.M. acknowledges a fellowship from Gutenberg Research College, Johannes Gutenberg University Mainz. E.C. acknowledges financial support from Comunidad de Madrid (2021-5A/AMB-20942), the European Union and from the Spanish Ministry of Science and Innovation (PID2019-107808RA-I00). IMDEA Nanociencia acknowledges support from the Severo Ochoa Programme for Centres of Excellence in R&D (MINECO, grant CEX2020-001039-S). S.G.-O. is grateful to the Spanish State Research Agency for a Ph.D. grant (FPI, PRE2019-09345). GMP thanks Fondazione Cariplo (Grant no. 2018-0979) for financial support. The IMDEA Nanociencia authors thank support from the European Research Council through the ERC-Synergy grant (TOMATTO).

References

1. Deenadayalan, M.S., Sharma, N., Verma, P.K., and Nagaraja, C.M. (2016) Visible-Light-Assisted Photocatalytic Reduction of Nitroaromatics by Recyclable Ni(II)-Porphyrin Metal-Organic Framework (MOF) at RT. *Inorg Chem*, **55** (11), 5320–5327.
2. Lu, W., Li, N., Chen, W., and Yao, Y. The role of multiwalled carbon nanotubes in enhancing the catalytic activity of cobalt tetraaminophthalocyanine for oxidation of conjugated dyes. *Carbon N Y*, **47** (14), 3337–3345.
3. Wang, A., Shen, X., Wang, Q., Cheng, L., Zhu, W., Shang, D., and Song, Y. (2021) Boosted charge transfer in porphyrin and zinc phthalocyanine co-functionalized graphene oxide nanohybrids toward improved optical limiting and H2 evolution. *Dyes and Pigments*, **187** (January), 109142.
4. Watanabe, M. (2017) Dye-sensitized photocatalyst for effective water splitting catalyst. *Sci Technol Adv Mater*, **18** (1), 705–723.
5. Park, J.H., and Bard, A.J. (2006) Photoelectrochemical tandem cell with bipolar dye-sensitized electrodes for vectorial electron transfer for water splitting. *Electrochemical and Solid-State Letters*, **9** (2), 5–9.
6. Youngblood, W.J., Anna Lee, S.H., Maeda, K., and Mallouk, T.E. (2009) Visible light water splitting using dye-sensitized oxide semiconductors. *Acc Chem Res*, **42** (12), 1966–1973.

7. Taranu, B.-O., and Fagadar-Cosma, E. (2022) The pH Influence on the Water-Splitting Electrocatalytic Activity of Graphite Electrodes Modified with Symmetrically Substituted Metalloporphyrins. *Nanomaterials*, **12** (21), 3788.
8. Choi, S., Kim, C.H., Baeg, J.O., Son, H.J., Pac, C., and Kang, S.O. (2020) Collisional Electron Transfer Route between Homogeneous Porphyrin Dye and Catalytic TiO2/Re(I) Particles for CO2Reduction. *ACS Appl Energy Mater*, **3** (12), 11581–11596.
9. Nguyen, T.V., Wu, J.C.S., and Chiou, C.H. (2008) Photoreduction of CO2 over Ruthenium dye-sensitized TiO2-based catalysts under concentrated natural sunlight. *Catal Commun*, **9** (10), 2073–2076.
10. Tasseroul, L., Páez, C.A., Lambert, S.D., Eskenazi, D., and Heinrichs, B. (2016) Photocatalytic decomposition of hydrogen peroxide over nanoparticles of TiO2 and Ni(II)-porphyrin-doped TiO2: A relationship between activity and porphyrin anchoring mode. *Appl Catal B*, **182**, 405–413.
11. Mandal, T., Das, S., and De Sarkar, S. (2019) Nickel(II) Tetraphenylporphyrin as an Efficient Photocatalyst Featuring Visible Light Promoted Dual Redox Activities. *Adv Synth Catal*, **361** (13), 3200–3209.
12. Liu, C., van den Bos, D., den Hartog, B., van der Meij, D., Ramakrishnan, A., and Bonnet, S. (2021) Ligand Controls the Activity of Light-Driven Water Oxidation Catalyzed by Nickel(II) Porphyrin Complexes in Neutral Homogeneous Aqueous Solutions. *Angewandte Chemie - International Edition*, **60** (24), 13463–13469.
13. Chen, G., Chen, L., Ng, S.M., and Lau, T.C. (2014) Efficient chemical and visible-light-driven water oxidation using nickel complexes and salts as precatalysts. *ChemSusChem*, **7** (1), 127–134.
14. Xu, J., Liu, X., Zhou, Z., and Xu, M. (2020) Photocatalytic CO2 reduction catalyzed by metalloporphyrin: Understanding of cobalt and nickel sites in activity and adsorption. *Appl Surf Sci*, **513**.
15. Ding, X., Yu, B., Han, B., Wang, H., Zheng, T., Chen, B., Wang, J., Yu, Z., Sun, T., Fu, X., Qi, D., and Jiang, J. (2022) Porphyrin Coordination Polymer with Dual Photocatalytic Sites for Efficient Carbon Dioxide Reduction. *ACS Appl Mater Interfaces*, **14** (6), 8048–8057.
16. Rong, J., Magdaong, N.C.M., Taniguchi, M., Diers, J.R., Niedzwiedzki, D.M., Kirmaier, C., Lindsey, J.S., Bocian, D.F., and Holten, D. (2021) Electronic Structure and Excited-State Dynamics of Rylene-Tetrapyrrole Panchromatic Absorbers. *Journal of Physical Chemistry A*, **125** (36), 7900–7919.
17. Yuen, J.M., Diers, J.R., Alexy, E.J., Roy, A., Mandal, A.K., Kang, H.S., Niedzwiedzki, D.M., Kirmaier, C., Lindsey, J.S., Bocian, D.F., and Holten, D. (2018) Origin of Panchromaticity in Multichromophore-Tetrapyrrole Arrays. *Journal of Physical Chemistry A*, **122** (36), 7181–7201.
18. Chen, Q., Brambilla, L., Daukiya, L., Mali, K.S., De Feyter, S., Tommasini, M., Müllen, K., and Narita, A. (2018) Synthesis of Triply Fused Porphyrin-Nanographene Conjugates. *Angewandte Chemie - International Edition*, **57** (35), 11233–11237.
19. Brogdon, P., Cheema, H., and Delcamp, J.H. (2018) Near-Infrared-Absorbing Metal-Free Organic, Porphyrin, and Phthalocyanine Sensitizers for Panchromatic Dye-Sensitized Solar Cells. *ChemSusChem*, **11** (1), 86–103.
20. Wolf, M., Lungerich, D., Bauroth, S., Popp, M., Platzer, B., Clark, T., Anderson, H.L., Jux, N., and Guldi, D.M. (2020) Panchromatic light funneling through the synergy in hexabenzocoronene-(metallo)porphyrin-fullerene assemblies to realize the separation of charges. *Chem Sci*, **11** (27), 7123–7132.
21. Shiu, J.W., Chang, Y.C., Chan, C.Y., Wu, H.P., Hsu, H.Y., Wang, C.L., Lin, C.Y., and Diau, E.W.G. (2015) Panchromatic co-sensitization of porphyrin-sensitized solar cells

to harvest near-infrared light beyond 900 nm. *J Mater Chem A Mater*, **3** (4), 1417–1420.
22. Wang, W.C., Lin, Y.W., Peng, S.H., Chuang, C.T., Chang, C.C., and Hsu, C.S. (2020) A strategy of designing near-infrared porphyrin-based non-fullerene acceptors for panchromatic organic solar cells. *Org Electron*, **86** (June), 105899.
23. Ballabio, M., and Cánovas, E. (2022) Electron Transfer at Quantum Dot-Metal Oxide Interfaces for Solar Energy Conversion. *ACS Nanoscience Au*, **2** (5), 367–395.
24. Patchkovskii, S., Kozlowski, P.M., and Zgierski, M.Z. (2004) Theoretical analysis of singlet and triplet excited states of nickel porphyrins. *Journal of Chemical Physics*, **121** (3), 1317–1324.
25. Chen, L.X., Zhang, X., Wasinger, E.C., Attenkofer, K., Jennings, G., Muresan, A.Z., and Lindsey, J.S. (2007) Tracking electrons and atoms in a photoexcited metalloporphyrin by X-ray transient absorption spectroscopy. *J Am Chem Soc*, **129** (31), 9616–9618.
26. Shelby, M.L., Lestrange, P.J., Jackson, N.E., Haldrup, K., Mara, M.W., Stickrath, A.B., Zhu, D., Lemke, H.T., Chollet, M., Hoffman, B.M., Li, X., and Chen, L.X. (2016) Ultrafast Excited State Relaxation of a Metalloporphyrin Revealed by Femtosecond X-ray Absorption Spectroscopy. *J Am Chem Soc*, **138** (28), 8752–8764.
27. Zhang, X., Wasinger, E.C., Muresan, A.Z., Attenkofer, K., Jennings, G., Lindsey, J.S., and Chen, L.X. (2007) Ultrafast stimulated emission and structural dynamics in nickel porphyrins. *Journal of Physical Chemistry A*, **111** (46), 11736–11742.
28. Eom, H.S., Jeoung, S.C., Kim, D., Ha, J.-H., and Kim, Y.-R. (1997) Ultrafast Vibrational Relaxation and Ligand Photodissociation / Photoassociation Processes of. *J. Phys. Chem. A*, **101** (20), 3661–3669.
29. Zamyatin, A. V., Soldatova, A. V., and Rodgers, M.A.J. (2007) The photophysics of Ni(II) meso-tetraphenylbenzoporphyrin: A combined theoretical and experimental investigation. *Inorganica Chim Acta*, **360** (3), 857–868.
30. Azenha, E.G., Serra, A.C., Pineiro, M., Pereira, M.M., Seixas de Melo, J., Arnaut, L.G., Formosinho, S.J., and Rocha Gonsalves, A.M. d. A. (2002) Heavy-atom effects on metalloporphyrins and polyhalogenated porphyrins. *Chem Phys*, **280** (1–2), 177–190.
31. Ryland, E.S., Zhang, K., and Vura-Weis, J. (2019) Sub-100 fs Intersystem Crossing to a Metal-Centered Triplet in Ni(II)OEP Observed with M-Edge XANES. *Journal of Physical Chemistry A*, (Ii).
32. Rodriguez, J., Kirmaier, C., and Holten, D. (1989) Optical Properties of Metalloporphyrin Excited States. *J Am Chem Soc*, **111** (17), 6500–6506.
33. Andersson, J., Puntoriero, F., Serroni, S., Yartsev, A., Pascher, T., Polívka, T., Campagna, S., and Sundström, V. (2004) Ultrafast singlet energy transfer competes with intersystem crossing in a multi-center transition metal polypyridine complex. *Chem Phys Lett*, **386** (4–6), 336–341.
34. Concepcion, J.J., House, R.L., Papanikolas, J.M., and Meyer, T.J. (2012) Chemical approaches to artificial photosynthesis. *Proc Natl Acad Sci U S A*, **109** (39), 15560–15564.
35. Ardo, S., and Meyer, G.J. (2009) Photodriven heterogeneous charge transfer with transition-metal compounds anchored to TiO2 semiconductor surfaces. *Chem Soc Rev*, **38** (1), 115–164.
36. Drain, C.M., Kirmaier, C., Medforth, C.J., Nurco, D.J., Smith, K.M., and Holten, D. (1996) Dynamic photophysical properties of conformationally distorted nickel porphyrins. 1. Nickel(II) dodecaphenylporphyrin. *Journal of Physical Chemistry*, **100** (29), 11984–11993.

37. Ting, S.I., Garakyaraghi, S., Taliaferro, C.M., Shields, B.J., Scholes, G.D., Castellano, F.N., and Doyle, A.G. (2020) 3d-d Excited States of Ni(II) Complexes Relevant to Photoredox Catalysis: Spectroscopic Identification and Mechanistic Implications. *ACS Appl Mater Interfaces*, (Ii).

The table of contents

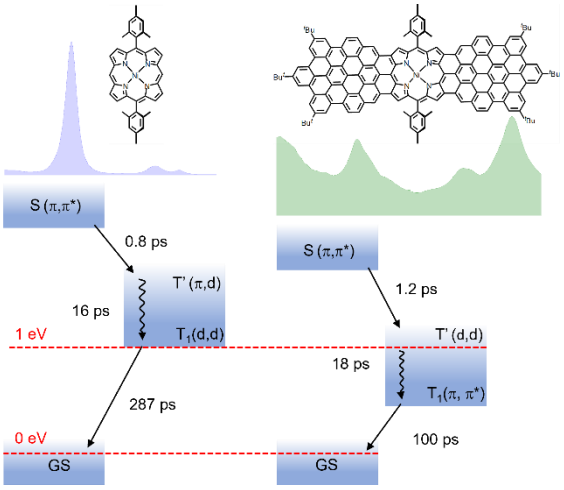

Extension of Ni-porphyrin with triply fused nanographenes leads to a conjugated planarized molecule exhibiting high panchromaticity. The nanographene moieties act as antennas during the electronic relaxation process towards an intermediate (d,d) triplet state almost unnaffected by the symmetric conjugation expansion, which subsequently delocalizes along the ligand.

Supporting Information

Nanographene based decoration as a panchromatic antenna for metalloporphyrin conjugates

Saül Garcia-Orrit,[a] Víctor Vega-Mayoral,[a] Qiang Chen,[b] Gianluca Serra,[c] Giuseppe M. Paternò,[d] Enrique Cánovas,[a] Akimitsu Narita,[b,e] Klaus Müllen,[b,f] Matteo Tommasini,[c] Juan Cabanillas-González,[a*]*

[a] Madrid Institute for Advanced Studies, IMDEA Nanociencia, c/Faraday 9, Campus de Cantoblanco, Madrid 28049, Spain.
[b] Max Planck Institute for Polymer Research, Ackermannweg 10, 55128 Mainz, Germany
[c] Dipartimento di Chimica, Materiali ed Ingegneria Chimica "G.Natta", Politecnico di Milano, Piazza Leonardo da Vinci 32, 20133 Milano (Italy)
[d] Physics Department, Politecnico di Milano, Piazza Leonardo Da Vinci, 32, 20133 Milano, Italy
[e] Organic and Carbon Nanomaterials Unit, Okinawa Institute of Science and Technology Graduate University, Okinawa 904-0495, Japan
[f] Institute for Physical Chemistry, Johannes Gutenberg University Mainz, Duesbergweg 10-14, 55128 Mainz, Germany

1. Experimental Section/Methods

TAS set-up

Femtosecond transient absorption spectroscopy measurements have been performed using a Ti:Sapphire laser with 120 fs pulse duration centered at 778 nm (~1.6 eV). The **NPN** absorbance at 778 nm is low and the obtained TAS signal performs a low signal to noise ratio, therefore TAS measurements were carried out by pumping at 605 nm, near the second absorbance resonance in the **NPN** spectra; a NOPA is employed to obtain the desired pumping wavelength. For **NiDMP**, as its lowest excited state is above the laser's fundamental emission, TAS measurements were performed by pumping with the second harmonic, i.e., 389 nm (3.19 eV) generated by a BBO crystal. Pump fluence is set at 0.65 $\mu J/cm^2$ for all the measurements, with a 0.4 μJ pulse with a diameter of 280 μm. Reported dynamics are in the linear regime (one e-h per molecule). The probed spectral window is given by the supercontinuum generated in a sapphire crystal (between 0.9 eV and 1.6 eV), enabling the study of electron dynamics around/in the vicinity of the HOMO-LUMO gaps of selected molecules. TAS measurements were carried out with 0.043 mM of **NiDMP** and 0.022 mM of **NPN.** These concentrations afforded a clear $\Delta T/T$ signal out of solution saturation regime. All samples were prepared in a nitrogen atmosphere at room temperature and ambient pressure.

Sample preparation

The synthesis procedure to obtain **NiDMP** and the **NPN** nanographene, as well as its high-resolution matrix-assisted laser desorption/ionization time-of-flight mass spectrometry (HR MALDI-TOF MS), IR and Raman spectroscopy, and scanning tunnelling microscopy (STM), have been previously explained and reported by Qiang Chen and coworkers.[1] **NPN** and **NiDMP** conjugates have been diluted using anhydrous solvents, this dilution is prepared inside a glovebox to preserve a nitrogen atmosphere and avoid possible photo-oxidation processes. Since **NPN** is a planar large molecule, in order to prevent aggregates, the dilution has been subjected to bath sonication for 12 minutes (with a temperature below 27 ºC) to properly disperse. To prepare our samples we employed chloroform solvent for the **NiDMP** and tetrahydrofuran (THF) solution for the **NPN** nanographene, the usage of THF instead of chloroform is justified by a better solubility of the compound in this solvent, in fact, **NPN** conjugate required 12 minutes of sonication to properly disolve in THF and prevent the presence of aggregates.

2. Transient Absorption Spectroscopy

1. Global fit analysis and singular value decomposition

A global fit analysis as previously described in detail by van Stokkum et al, [2] has been applied to model the TAS signal decay among the different probe wavelengths. In short, the validity of the Beer Lambert law is assumed (system is far from saturated absorption at all probe energies):

$$A(t,w) = \sum_i C_i(t) \cdot \sigma_i(w) \quad \text{(S1)}$$

to reproduce the measured transient absorption spectrum *A(t,w)*, which depends on time *t* and angular frequency *w* (*w* = 1242 eV·nm/λ with λ the wavelength in nm), as a superposition of *i* excited state transitions with characteristic time-resolved concentration *Ci(t)* and energy resolved absorption cross-section *σ(w)*. Equation S1 can be written in matrix form:

$$A(t,w) = C \cdot \sigma \quad \text{(S2)}$$

In Equation S2, each column of the *C* matrix represents one complete concentration-time dependence of a state *i*, while each row of the σ matrix represents the full (time-invariant) spectrum of that state *i*, and is known as evolution-associated difference spectra (EADS).

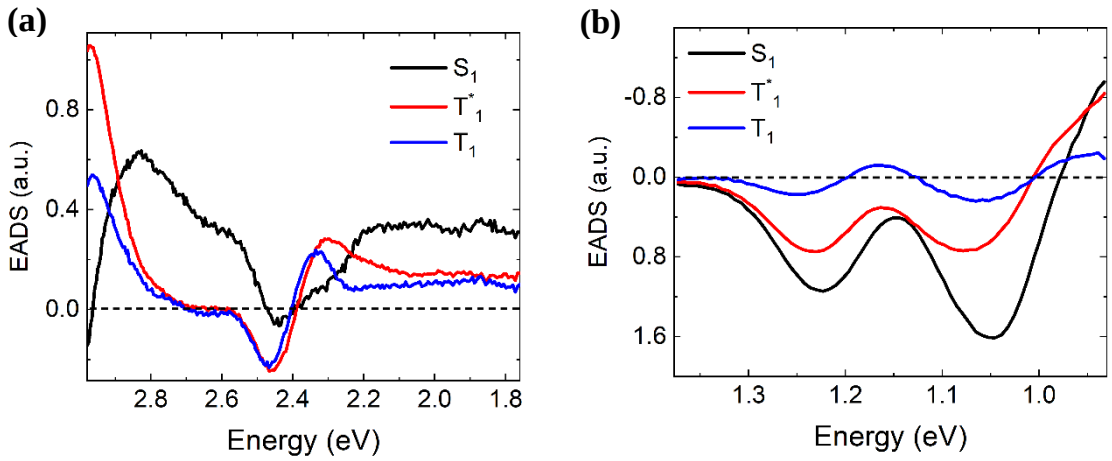

Figure S1. EADS obtained from the Global fit analysis applied to the TAS measurements for **(a) NiDMP** and **(b) NPN** molecules.

For **NiDMP** we employed a model based on a previously reported similar porphyrin (**NiTMP**) [3]. This model is based in a four sequential level scheme, represented by the first singlet state (S*), which undergoes inter-system crossing to an upper triplet level (T´), followed by thermalization to the lowest triplet level (T_1), which finally decays to the ground state (GS). By applying this model by global fit analysis, we reproduce the TAS signal, being the associated EADS plotted in **Figure S1a**, together with the residuals Figure S3. In figure S1 we can clearly observe the presence of the first derivative-like feature in the last two states, which involve the T´ and T_1 levels respectively, while this feature is not present in the singlet signature.

Nevertheless, for **NPN** conjugate there is no previous literature on its electron kinetics, therefore, in a first step, singular value decomposition (SVD) is deployed to estimate the number of states that need to be considered in Equation S2. SVD is based on in a matrix A can be expressed as the product of three matrixes:

$$A = U \cdot \Gamma \cdot V \qquad (S3)$$

Where Σ is a diagonal matrix and represents a translation, and U and V are rotation matrixes. Nevertheless, if det(A) $\neq$ 0 this decomposition is no longer valid, and a singular value

decomposition (SVD) is needed. SVD allows us to obtain A as sum of rank 1 matrices, so we can approximate A to the sum of the terms with the higher contribution, if A is a rank n matrix it can be expressed as:

$$A = \sum_{i,j,k=1}^{n} U_{ij} \cdot \gamma_i \cdot V_{ki} \quad \text{(S4)}$$

where *U* and *V* are the vector and convector matrices respectively, and γ_i are the singular values contained at the diagonal matrix Λ. If $\gamma_k << 1$, for example, then the equation ... can be approximated as:

$$A \approx \sum_{i,j,k=1}^{3} U_{ij} \cdot \gamma_i \cdot V_{ki} \quad \text{(S5)}$$

Therefore, if A represents the TAS measurement matrix, then γ_i are the Singular Values we are interested in. If we apply this decomposition to the **NPN** TAS matrix the γ_i values presented at **Figure S2** are obtained.

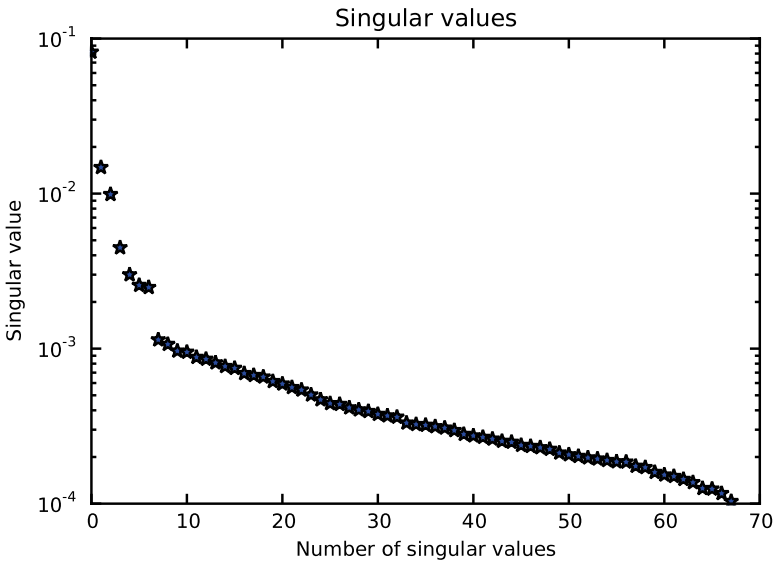

Figure S2. Singular values obtained when decomposing the measured TAS matrix of **NPN** molecule. These mathematical results represent the spectral weight associated to a certain excited state.

As we can observe the first three values are above 10^{-2}, and there is a wide gap between γ_3 and γ_4 and another one between γ_7 and γ_8. This indicates that the first three values have the strongest contribution, and intermediate values between the gaps do not contribute

significantly, i.e., to obtain a variance in the matrix representations we should consider or the first three singular values, the first four or the first eight. As each γ_i represents a different state of the excited molecule, consider eight states is physically misleading as internal conversion occurs faster than the instrumental response function of the system, therefore only states near S_1 will contribute to the electron kinetics, that is why we expect to reconstruct the TAS matrix approximating A with the first three singular values (as presented in **Figure S3a.1.2**) and an enhancement if the fourth singular value is added (**Figure S3b.1.2**). Hence, these calculations have allowed us to estimate the number of states involved during the de-excitation process. However, the kinetic model employed to describe the excited state must be physically justified, SVD only provides a mathematical tool but not a physical interpretation.

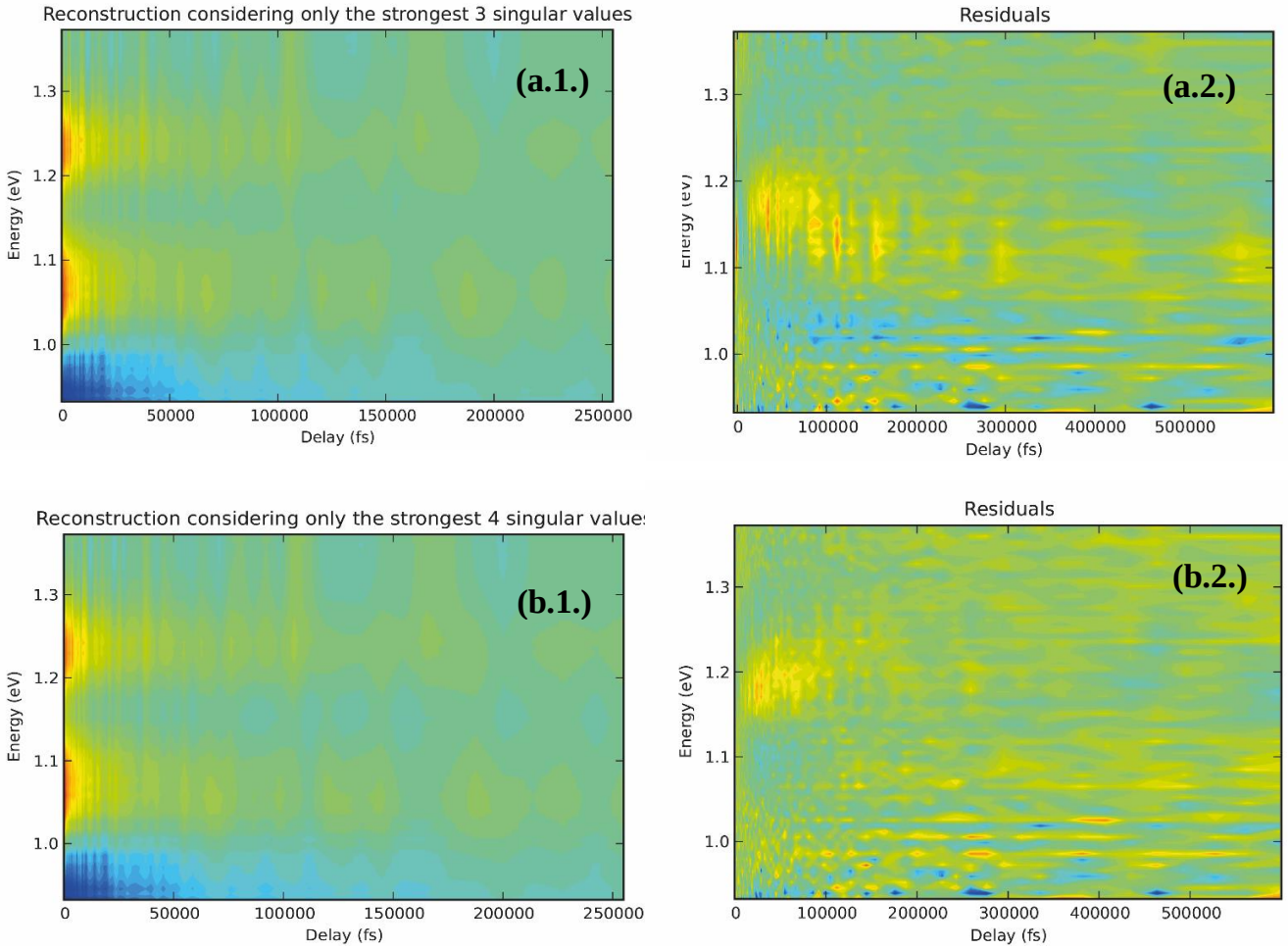

Figure S3. Reconstructed ΔT/T spectra over time considering the first three **(a.1.)** and four **(b.1.)** singular values and the respective residuals obtained for each reconstruction **(a.2.)** and **(b.2.)**.

As previously described in the main text, the same four sequential level model was applied to reconstruct the **NPN** TAS signal, the comparison between the time traces and the contour-plots are presented in the main text in Figure 2 and Figure 3 respectively. Therefore, this model will consider the 3 excited states presented in the EADS, associated to the Global fit analysis, in FigureS1b. The residuals obtained for both, **NiDMP** and **NPN**, is shown in **Figure S4**.

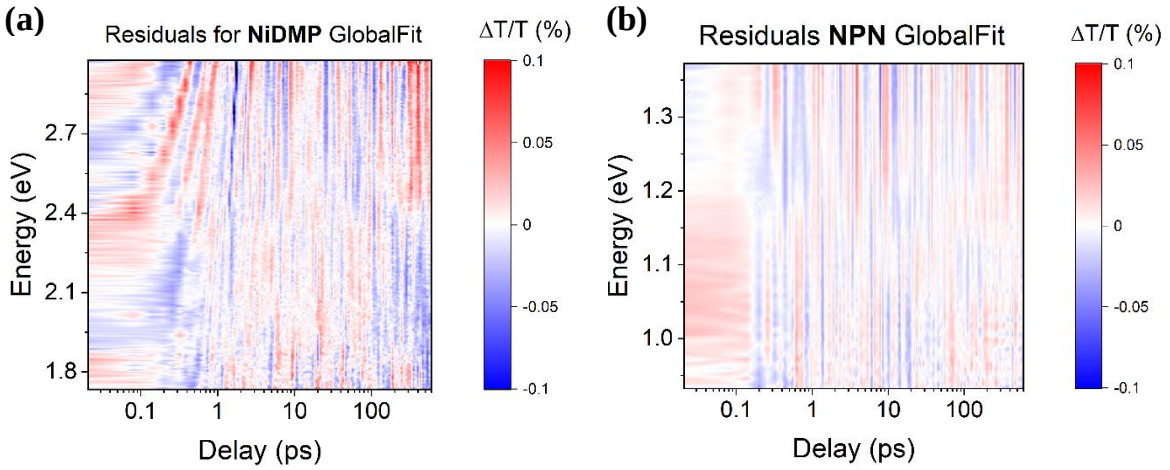

Figure S4. Residuals obtained applying the Global fit analysis with a four sequential model for **NiDMP (a)** and **NPN (b)** conjugates.

Finally, we also present the TAS spectra measured at different pump-probe delays. For the **NiDMP** we can clearly observe the mentioned first-derivative like feature (**Figure S5a**). And for **NPN** that GSB is dominating the kinetics in this system despite the excited state absorption at 0.97 eV (**Figure S5b**).

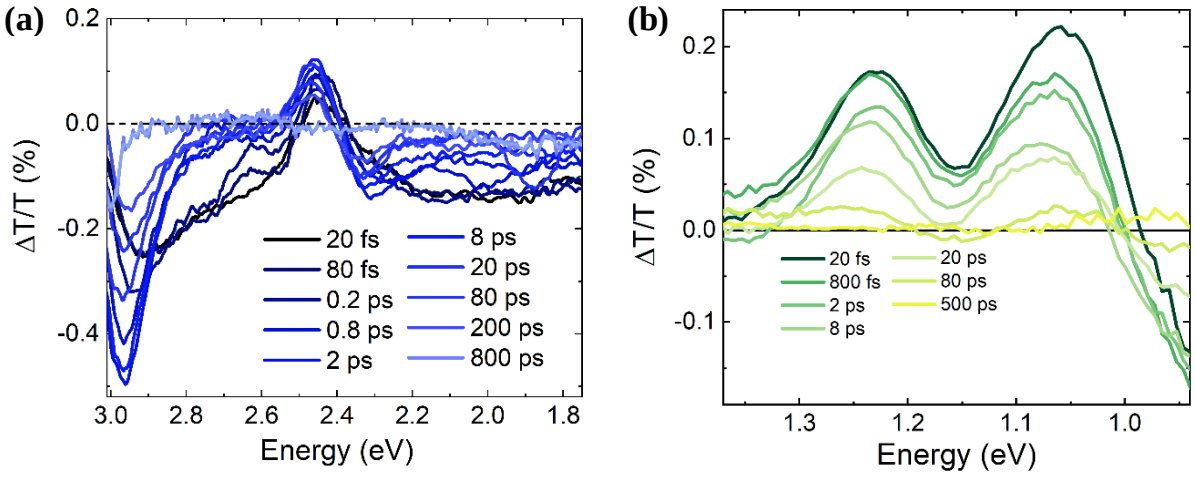

Figure S5. ΔT/T signal obtained at different wavelengths and pump-probe delays measured for **NiDMP (a)** and **NPN (b)** molecules.

3. Quantum chemical calculations

Density functional theory (DFT) and time dependent DFT (TDDFT) calculations have been performed using the Gaussian09 program [4]. We followed the computational approach introduced by Patchkovskii et al. to interpret the singlet and triplet states of Ni porphyrins [5]. This method, which is substantially equivalent to that used in similar studies [3], correctly predicts the peak positions of the Soret band of **NiDMP**, measured at 401 nm, and the less intense feature at 515 nm, and it was thus selected for calculating molecular orbitals and excited states of both **NiDMP** and **NPN**. Briefly, the structures of **NiDMP** and **NPN** were first optimized by using the B3LYP functional and the 6-31G(d,p) basis set for hydrogen, carbon, and nitrogen, and the Ahlrichs VTZ basis set for nickel [6]; on such structures TDDFT calculations have been carried out with the PBE functional, whose performance in predicting excitation energies is very close to that of the BP86 functional used in ref. [5], as expected from extensive benchmark calculations [7], and as verified in this work for the **NiDMP** compound (see below). The triplets were assessed with the same TDDFT calculations. The optimized structure of the lowest lying S_1 state of **NPN** was computed by the TDDFT approach. The stability of the B3LYP equilibrium structures of **NPN** and **NiDMP** was confirmed by the absence of negative eigenvalues of the Hessian. The wavelengths and oscillator strengths of 150 and 500 excited states were computed respectively for **NiDMP** and **NPN** (the different number of computed states reflects the different molecular size); then, UV-Vis spectra were obtained with the procedure described in reference [8] assuming a FWHM of 0.1 eV (this simulation of the spectra is close to summing Lorentzian functions centered at the computed wavelengths with their heights proportional to the oscillator strengths).

Selection of the DFT functional. To evaluate the effects of the choice of the DFT functional we computed the absorption spectrum of an isolated **NiDMP** molecule using several widely used functionals, namely B3LYP, M06, BP86 [9], CAM-B3LYP [10], PBE [11], and wB97XD [12]. The absorption spectra (**Figure S6** and **Figure 1** of the main text) have been simulated from the results of TDDFT calculations with the procedure described in [8] and a FWHM of 0.1 eV. As shown in **Figure S6**, the best agreement with the observed spectrum is obtained with the PBE and the BP86 functionals, which produce almost identical results, and also account for the presence of excitations in correspondence of the Q band (experimental features at 515 and 548 nm), although such transitions are computed with an intensity that is much smaller than experimentally observed. The spectra of **NiDMP** simulated with the PBE

and BP86 functionals also show bands in the region between 300 and 400 nm which are very weak in the measured spectrum. However, when considering (at the PBE level) the explicit interaction of the Ni centre with two chloroform molecules (the solvent used in the experiments), we observe that such features substantially reduce their intensity ratio with respect to the Soret transition. We therefore ascribe the bands between 300 and 400 nm to the absence of solvent effects in the isolated **NiDMP** model and choose PBE as a reliable functional for further quantum chemical studies. Since solvent effects are apparently just modulating the transition strengths below 400 nm, for the sake of keeping the computational efforts under control we consider in the following just calculations on isolated molecules.

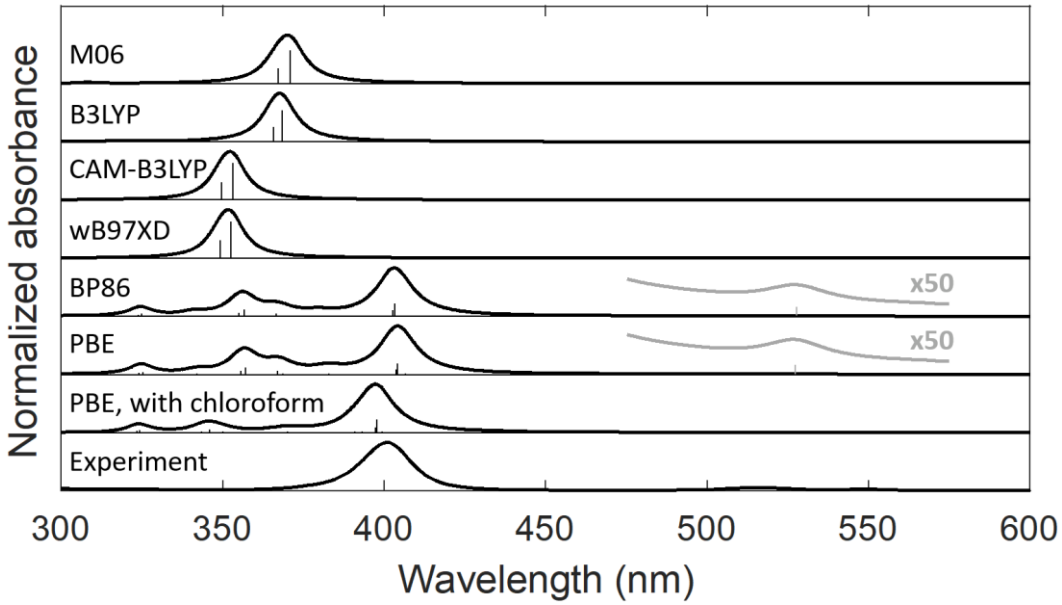

Figure S6. Computed and experimental spectra of **NiDMP**. The intensity of each spectrum has been normalized to one. Parts of the spectra computed by the BP86 and PBE functionals have also been multiplied by 50 after normalization for more clarity. Black lines indicate the position of the computed vertical transitions whose oscillator strengths are proportional to the line height; grey lines have the same meaning but refer to the zoomed parts of the spectra.

Optimized structures. Figure S7 shows the optimized structures of the molecular models of **NiDMP** (both isolated and interacting with two chloroform molecules) and **NPN**. The equilibrium structure of **NiDMP** is slightly nonplanar, in accordance with a previous work [5]. This is contrary to the case of **NPN**, where the inner porphyrin core is coupled with highly conjugated and planar graphene moieties that impose an overall planarity on such extensively π-conjugated molecule.

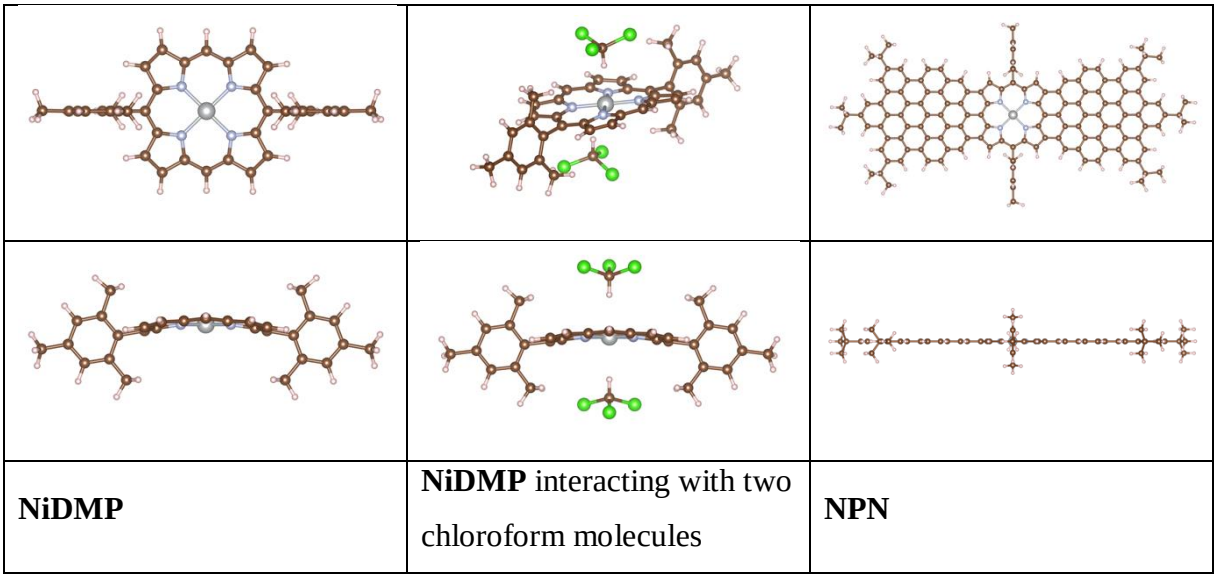

NiDMP	**NiDMP** interacting with two chloroform molecules	**NPN**

Figure S7. Equilibrium geometries of the molecular models used in this study: **NiDMP** (left), **NiDMP** interacting with two chloroform molecules (centre), and **NPN** (right).

Main transitions in the UV-vis spectra. In **Table S1** we assign the main features of the measured absorption spectrum of **NiDMP** (shown both in Figure 1 in the main text and in **Figure S6**) namely the Soret band at about 401 nm and the two less intense features in the Q band region, at 515 and 548 nm. The Soret band is mainly due to the HOMO-4 → LUMO+2 and the HOMO-3 → LUMO+1 electronic excitations. The Q band at 515 nm is assigned to HOMO-4 → LUMO+2, HOMO-3 → LUMO+1. In analogy with other porphyrins [13], the band at 548 nm is assigned to the 0→1 vibronic component of the Q band at 515 nm (which is the 0→0 transition). Since our present TDDFT calculations do not consider vibronic couplings, this band is absent in the simulated spectra, like the case of the 994 nm band of **NPN** (see below). **Table** S1 also displays the rendering of the molecular orbitals involved in the mentioned transitions.

Experimental peak position (nm)	Computed wavelength and energy	Oscillator strength	Assigned transitions	
401	404 nm, 3.07 eV	0.4576	HOMO-4 → LUMO+2	0.40
			HOMO-3 → LUMO+1	0.34
517	527 nm, 2.35 eV	0.0041	HOMO-4 → LUMO+2	-0.46
			HOMO-3 → LUMO+1	0.53
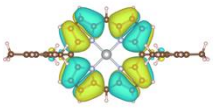	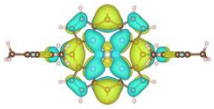	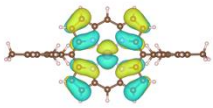	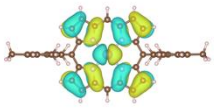	
HOMO-4	HOMO-3	HOMO-2	HOMO-1	
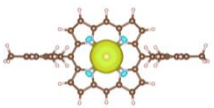	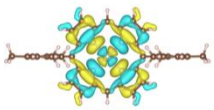	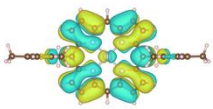	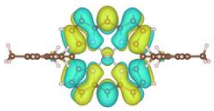	
HOMO	LUMO	LUMO+1	LUMO+2	

Table S1. Assignment of the main features of the absorption spectrum of **NiDMP** resulting from TDDFT computations. The relative contribution of each transition to the excited state computed by TDDFT is also reported in the last column. The bottom part of the Table shows isosurfaces at 0.012 $a_0^{-3/2}$ of the molecular orbitals of **NiDMP** involved in the transitions.

The measured absorption spectrum of **NPN** is compared with the simulated one in **Figure 1** of the main text and its main bands are assigned in **Table S2**. The features at 605 nm and at 1173 nm are well reproduced by our calculation. The band at 605 nm is related to two close states described by HOMO-6 → LUMO+3, HOMO → LUMO+6, and by HOMO-7 → LUMO+2, and HOMO-4 → LUMO+3 transitions. The band at 1173 nm is assigned to the HOMO → LUMO transition. The feature at 994 nm (1.25 eV), not predicted by our calculation, is assigned to the 0-1 vibronic transition of the S_1 state: indeed, its energy spacing with the feature at 1173 nm (1.05 eV) is compatible with a vibrational wavenumber of about 1610 cm^{-1}, which is fully compatible with a G peak mode that is known to be vibronically coupled with π-π* excitations from Raman investigations on graphene molecules with similar shape and symmetry [14]. Such vibronic feature is not predicted by TDDFT calculations at the Franck-Condon point, such as those considered in the present work.

Experimental peak position (nm)	Computed wavelength and energy	Oscillator strength	Assigned transitions	
605	575 nm, 2.15 eV	0.76	HOMO-6 → LUMO+3	0.43
			HOMO → LUMO+6	0.37
	610 nm, 2.03 eV	0.71	HOMO-7 → LUMO+2	0.38
			HOMO-4 → LUMO+3	0.47
1173	1143 nm, 1.08 eV	1.54	HOMO → LUMO	0.69

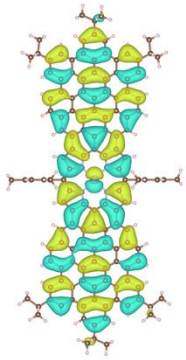	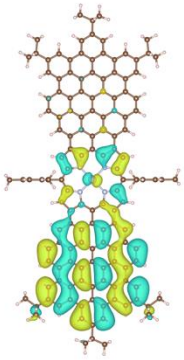	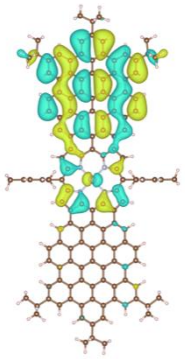	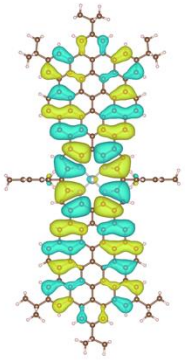	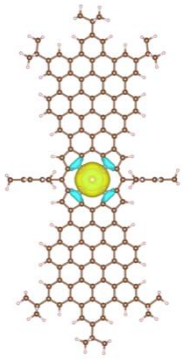
HOMO-7	HOMO-6	HOMO-5	HOMO-4	HOMO-3
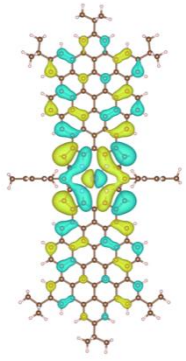	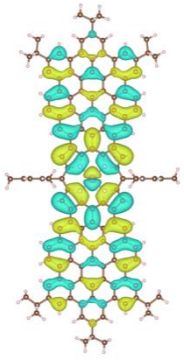	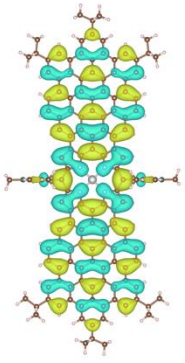	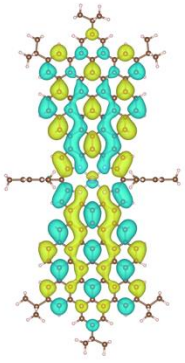	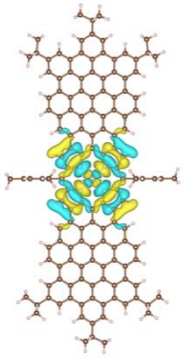
HOMO-2	HOMO-1	HOMO	LUMO	LUMO+1
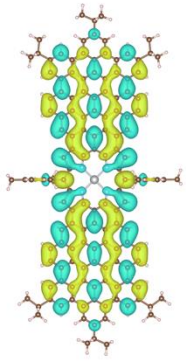	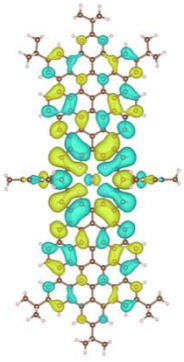	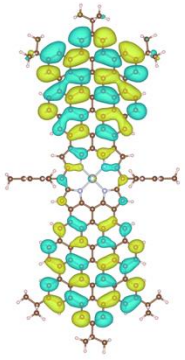	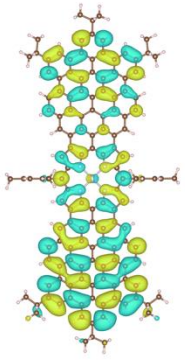	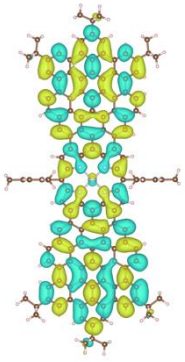
LUMO+2	LUMO+3	LUMO+4	LUMO+5	LUMO+6

Table S2. Assignment of the main features of the absorption spectrum of **NPN** based on results from TDDFT computations. The relative contribution of each transition to the excited state computed by TDDFT is also reported in the last column. The bottom part of the Table shows isosurfaces at 0.006 $a_0^{-3/2}$ of the molecular orbitals of **NPN** involved in the transitions.

Finally, we show in **Figure S8** the equilibrium bond length differences between the optimized structure of the ground state and the S_1 state of **NPN**. For consistency in the calculation of the bond length difference we used the same PBE functional in the DFT optimization of the ground state and in the TDDFT optimization of S_1. Clearly, the structure change between the ground state and S_1 involves many CC bonds of the **NPN** molecule.

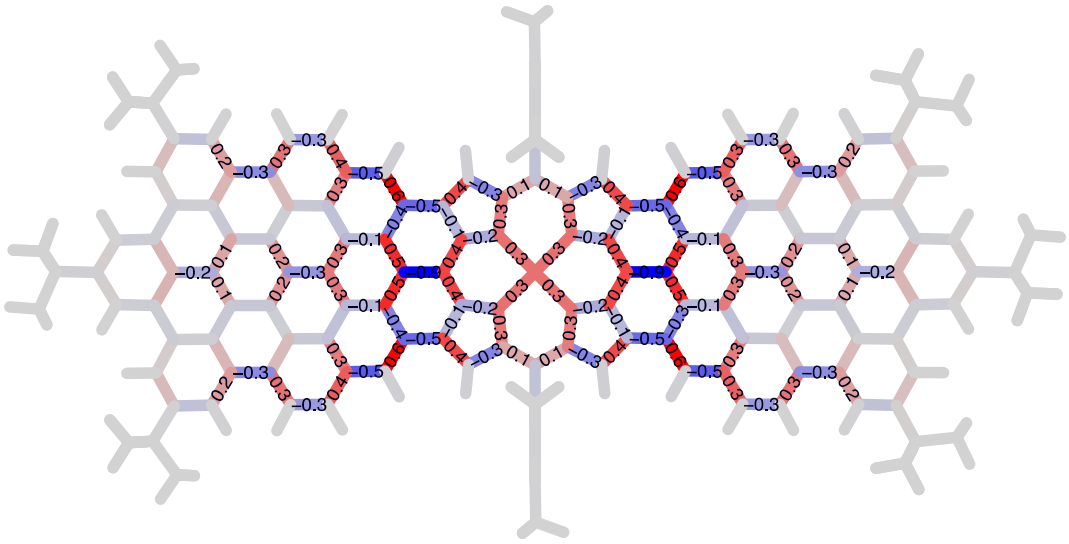

Figure S8. Pattern of the bond length changes (pm) computed between the minimum of the S_1 state and the minimum of the ground state of **NPN**.

References:

1. Chen, Q., Brambilla, L., Daukiya, L., Mali, K.S., De Feyter, S., Tommasini, M., Müllen, K., and Narita, A. (2018) Synthesis of Triply Fused Porphyrin-Nanographene Conjugates. *Angewandte Chemie - International Edition*, **57** (35), 11233–11237.
2. van Stokkum, I.H.M., Larsen, D.S., and van Grondelle, R. (2004) Global and target analysis of time-resolved spectra. *Biochim Biophys Acta Bioenerg*, **1657** (2–3), 82–104.
3. Shelby, M.L., Lestrange, P.J., Jackson, N.E., Haldrup, K., Mara, M.W., Stickrath, A.B., Zhu, D., Lemke, H.T., Chollet, M., Hoffman, B.M., Li, X., and Chen, L.X. (2016) Ultrafast Excited State Relaxation of a Metalloporphyrin Revealed by Femtosecond X-ray Absorption Spectroscopy. *J Am Chem Soc*, **138** (28), 8752–8764.
4. M. J. Frisch, G. W. Trucks, H. B. Schlegel, G. E. Scuseria, M. A. Robb, J. R. Cheeseman, G. Scalmani, V. Barone, G. A. Petersson, H. Nakatsuji, X. Li, M. Caricato, A. Marenich, J. Bloino, B. G. Janesko, R. Gomperts, B. Mennucci, H. P. Hratchian, J. V. Ort, and D.J.F. (2016) Gaussian 09, Revision A.02. *Gaussian 09, Revision A.02*.
5. Patchkovskii, S., Kozlowski, P.M., and Zgierski, M.Z. (2004) Theoretical analysis of singlet and triplet excited states of nickel porphyrins. *Journal of Chemical Physics*, **121** (3), 1317–1324.
6. Pritchard, B.P., Altarawy, D., Didier, B., Gibson, T.D., and Windus, T.L. (2019) New Basis Set Exchange: An Open, Up-to-Date Resource for the Molecular Sciences Community. *J Chem Inf Model*, **59** (11), 4814–4820.
7. Jacquemin, D., Wathelet, V., Perpète, E.A., and Adamo, C. (2009) Extensive TD-DFT benchmark: Singlet-excited states of organic molecules. *J Chem Theory Comput*, **5** (9), 2420–2435.
8. Zanchi, C., Longhi, G., Abbate, S., Pellegrini, G., Biagioni, P., and Tommasini, M. (2019) Evaluation of molecular polarizability and of intensity carrying modes contributions in circular dichroism spectroscopies. *Applied Sciences (Switzerland)*, **9** (21).
9. Becke, A.D. (1988) Density-functional exchange-energy approximation with correct asymptotic behavior. *Phys. Rev. A*, **38** (6), 3098–3100.
10. Yanai, T., Tew, D.P., and Handy, N.C. (2004) A new hybrid exchange-correlation functional using the Coulomb-attenuating method (CAM-B3LYP). *Chem Phys Lett*, **393** (1–3), 51–57.
11. Perdew, J.P., Burke, K., and Ernzerhof, M. (1997) Generalized Gradient Approximation Made Simple (vol 77, pg 3865, 1996). *Phys Rev Lett*, **78** (7), 1396–1396.
12. Chai, J. da, and Head-Gordon, M. (2008) Long-range corrected hybrid density functionals with damped atom-atom dispersion corrections. *Physical Chemistry Chemical Physics*, **10** (44), 6615–6620.
13. Song, Y., Schubert, A., Maret, E., Burdick, R.K., Dunietz, B.D., Geva, E., and Ogilvie, J.P. (2019) Vibronic structure of photosynthetic pigments probed by polarized two-dimensional electronic spectroscopy and ab initio calculations. *Chem Sci*, **10** (35), 8143–8153.
14. Maghsoumi, A., Brambilla, L., Castiglioni, C., Müllen, K., and Tommasini, M. (2015) Overtone and combination features of G and D peaks in resonance Raman spectroscopy of the C78H26 polycyclic aromatic hydrocarbon. *Journal of Raman Spectroscopy*, **46** (9), 757–764.